Title

Erratum: “Quantum-state Dependence of Product Branching Ratios in Vacuum Ultraviolet Photodissociation of N2” (2016, ApJ, 819, 23)

Journal

The Astrophysical Journal, 854(2)

ISSN

0004-637X

Authors

Song, Yu
Gao, Hong
Chang, Yih Chung
et al.

Publication Date

2018-02-20

DOI

10.3847/1538-4357/aaacfe

Peer reviewed

The Astrophysical Journal, 819:23 (13pp), 2016 March 1 doi:10.3847/0004-637X/819/1/23

QUANTUM-STATE DEPENDENCE OF PRODUCT BRANCHING RATIOS IN VACUUM ULTRAVIOLET PHOTODISSOCIATION OF N_2

Yu Song[1,4], Hong Gao[1,4,5], Yih Chung Chang[1], D Hammouténe[2], H. Ndome[3], M. Hochlaf[3], William M. Jackson[1], and C. Y. Ng[1]

[1] Department of Chemistry, University of California, Davis, CA 95616, USA; wmjackson@ucdavis.edu, cyng@ucdavis.edu
[2] Laboratoire de Thermodynamique et Modélisation Moléculaire, Faculté de Chimie, USTHB, BP32 El Alia, 16111 Bab Ezzouar, Alger, Algeria
[3] Université Paris-Est, Laboratoire Modélisation et Simulation Multi Echelle, MSME UMR 8208 CNRS, 5 bd Descartes, F-77454 Marne-la-Vallée, France
Received 2015 October 30; accepted 2016 January 19; published 2016 February 24

ABSTRACT

The branching ratios for the $N(^4S) + N(^2D)$, $N(^4S) + N(^2P)$, and $N(^2D) + N(^2D)$ channels are measured for the photodissociation of $N_2(X^1\Sigma_g^+; v'' = 0, J'')$ in the vacuum ultraviolet (VUV) region of 100,808–122,159 cm^{-1} using the VUV–VUV pump-probe approach combined with velocity-map-imaging-photoion detection. No evidence of forming the ground-state $N(^4S) + N(^4S)$ products is found. No potential barrier is observed for the $N(^2D) + N(^2D)$ channel, but the $N(^4S) + N(^2P)$ channel has a small potential barrier of ≈740 cm^{-1}. The branching ratios are found to depend on the symmetry of predissociative N_2 states instead of the total VUV excitation energy, indicating that N_2 photodissociation is nonstatistical. When the branching ratios for $N(^4S) + N(^2D)$ and $N(^4S) + N(^2P)$ products are plotted as a function of the VUV excitation energy for the valence N_2 $^1\Pi_u$ and $^1\Sigma_u^+$ states, oscillations in these ratios are observed demonstrating how these channels are competing with each other. These data can be used to select both the velocity and internal states of the atomic products by picking the quantum state that is excited. High-level ab initio potential energy curves of the excited N_2 states are calculated to provide insight into the mechanisms for the observed branching ratios. The calculations predict that the formation of both $N(^4S) + N(^2D)$ and $N(^4S) + N(^2P)$ channels involves potential energy barriers, in agreement with experimental observations. A discussion of the application of the present results to astronomy, planetary sciences, and comets is given.

Key words: ISM: kinematics and dynamics – ISM: molecules – methods: laboratory: molecular – molecular data – ultraviolet: ISM

1. INTRODUCTION

Nitrogen molecules are important in planetary and astronomical sciences because of the relatively large N_2/H_2 universal abundance ratio of 1.6×10^{-4}. The N_2 molecule dominates the atmospheres of Earth (Meier 1991; Feldman et al. 2001), Titan (Strobel & Shemansky 1982), and extrasolar planets (Moses et al. 2011). It also protects Earth from high-energy vacuum ultraviolet (VUV) radiation, and it plays a major role in the chemistry of the thermosphere (Torr & Torr 1979, 1982). The photochemistry of N_2 in a variety of environments, e.g., the interstellar medium, extrasolar planets, and circumstellar envelops, is believed to be responsible for the synthesis of N-containing molecules that are precursors to larger molecules that are the building blocks of life (Knauth et al. 2004; Snow 2004; van Dishoeck 2006; Balucani 2012; Li et al. 2013, 2014).

Listed below are Reactions (1)–(4) with their energetic thresholds that can occur when N_2 molecules absorb high-energy VUV radiation in the energy [$h\nu$(VUV)] range of $\leqslant$122,159 cm^{-1}:

$$N_2(X^1\Sigma_g^+) + h\nu(\mathrm{VUV}) \rightarrow N(^4S) + N(^4S) \quad h\nu(\mathrm{VUV}) \geqslant 78,\,714\ cm^{-1} \tag{1}$$

$$\rightarrow N(^4S) + N(^2D) \quad h\nu(\mathrm{VUV}) \geqslant 97,\,938\ cm^{-1} \tag{2}$$

$$\rightarrow N(^4S) + N(^2P) \quad h\nu(\mathrm{VUV}) \geqslant 107,\,553\ cm^{1} \tag{3}$$

$$\rightarrow N(^2D) + N(^2D) \quad h\nu(\mathrm{VUV}) \geqslant 117,\,162\ cm^{-1}. \tag{4}$$

The long radiative lifetimes and high internal energies of the excited $N(^2D)$ and $N(^2P)$ atomic photoproducts suggest that these atoms are highly reactive with other molecules, such as H_2, in low-pressure space environments (Balucani 2012). By comparison, the reactivity of ground-state $N(^4S)$ atoms toward H_2 molecules is known to be very low (Herron 1999). Thus, understanding the mechanisms for the formation of excited $N(^2D)$ and $N(^2P)$ atoms from N_2 photodissociation plays a pivotal role in modeling the chemistry occurring in astronomical environments.

A fast-beam experiment (Helm & Cosby 1989; Walter et al. 1993, 1994) investigated the N_2 photochemistry in the energy range of 110,175–112,918 cm^{-1}, which is significantly narrower than the present experimental range of 100,808–122,159 cm^{-1}. This group also reported additional branching ratio information on Reactions (2) and (3) at an American Geophysical Union Meeting in 1996 (Cosby & Walter 1996). The same experimental technique has also been used by Buijsse & van der Zande (1997a, 1997b) to investigate the predissociation dynamics of $N_2(c_4{}^1\Pi_u,\ v' = 0)$ and $N_2(b'^1\Sigma_u^+;\ v' = 16)$ states. The sensitivity of the fast-beam experiment is partly constrained by the high velocity of the N_2 beam required for coincident detection of N-atom products, but they were able to identify the formation of the spin-forbidden product channels (Reactions (2) and (3)). Nevertheless, these previous studies did not detect Reaction (4), and they mainly reported branching ratios for high J' levels owing to their experimental conditions. Besides the above photofragmentation

[4] These authors contributed equally to this work.
[5] Present address: Department of Chemistry, University of Basel, Klingelbergstrasse 80, 4056 Basel, Switzerland.

experiments, a high-resolution absorption spectroscopy method has long been used to study the photodissociation dynamics of N_2 (Carroll & Collins 1969; Dressler 1969; Yoshino et al. 1975). Recently, very accurate theoretical calculations using the coupled-channel Schrödinger equation (CSE) method have been performed by Lewis et al. (2005, 2008b) in a relatively low energy region and revealed Rydberg–Rydberg, Rydberg-valence, and singlet-triplet interactions in the predissociation process of N_2.

Earlier, a tunable VUV laser combined with a time-slice velocity-map imaging photoion (VMI-PI) detection was used to both photodissociate N_2 molecules in 109,369–109,611 cm^{-1} and ionize nascent N(^{2}D) photoproduct atoms (Gao et al. 2011; Pan et al. 2011). This apparatus has been augmented with a second tunable VUV laser source, and with it, the VUV photoexcitation of N_2 molecules and the VUV photoionization detection of product N atoms can be independently optimized (Song et al. 2012; Gao et al. 2013), increasing the experimental sensitivity. The motivations for this work are to provide the data needed for modelers of the various space environments described above and the benchmarks for state-of-the-art ab initio calculations of the potential energy curves (PECs), as well as for dynamics calculations on them.

The VUV absorption spectrum of N_2 is complicated partly because of the large number of valence and Rydberg states with different multiplicities. Many of the previously studied excited states have been classified into the two main vibrational progressions corresponding to the predissociative $N_2(b^1\Pi_u; v' = 0–23, J')$ and $N_2(b'^1\Sigma_u^+; v' = 0–28, J')$ valence states (Carroll & Collins 1969; Dressler 1969). Interspersed between these valence states are predissociative Rydberg states with the same symmetries, such as $N_2(c_n,o_n\ ^1\Pi_u; v', J')$ and $N_2(c'_n,^1\Sigma_u^+; v', J')$, which can also be reached by one-photon VUV excitations.

2. EXPERIMENTAL CONSIDERATION

The VUV–VUV laser VMI-PI apparatus used for the present study has been previously reported in detail (Song et al. 2012; Gao et al. 2013; Lu et al. 2014), so only a brief description is given here. The apparatus consists of two independently tunable VUV lasers coupled to a VMI-PI detector. A pulsed supersonic molecular beam of N_2 is generated through a pulsed valve (Even-Lavie Model: EL-5-2004, nozzle diameter = 0.2 mm) operating at 30 Hz and a total stagnation pressure of 30 psi. It is then skimmed and collimated by two skimmers before being crossed perpendicularly in the interaction region of the VMI-PI apparatus by two opposing unfocused VUV laser beams designated as VUV_1 and VUV_2. The supersonically cooled N_2 molecules in the interaction region are mostly in the $N_2(X^1\Sigma_g^+; v'' = 0; J'' = 0)$ state, so that one-photon excitation by the VUV_1 laser beam will only excite the molecule to ungerade predissociative rovibronic states. The VUV_2 laser beam is tuned to selectively photoionize the N(^{2}D) or N(^{4}S) atomic photofragments. Using two-photon resonance-enhanced four-wave mixing schemes employing a pulsed Kr or Xe gas jet as the nonlinear medium generates the tunable VUV laser beams. This produces VUV outputs at the sum and difference-frequencies $2\omega_1 \pm \omega_2$, where ω_1 and ω_2 are the fundamental UV and VIS frequencies, respectively. The $2\omega_1$ represents the two-photon UV resonant frequency fixed at a selected Kr or Xe electronic transition. The VIS ω_2 frequency is tunable to cover the VUV sum-frequency ($2\omega_1 + \omega_2$) output required for the experiment. The VUV laser output was measured to have an optical bandwidth of 0.4 cm^{-1} (FWHM). The typical delay time between the arrival of the VUV_1 photodissociation and the VUV_2 photoionization lasers at the interaction region is 10–20 ns.

The N(^{4}S) atoms were detected by the VUV_2 laser employing the VUV-VIS ($1 + 1'$) ionization scheme. In this scheme, the VUV_2 excitation of $N^*[2s^22p^2(^3P)4d] \leftarrow N(^4S)$ is followed by photoionization of the excited state using the VIS ω_2 laser that is also present in the interaction region. The N(^{2}D) fragments are detected by tuning the VUV_2 laser to excite N(^{2}D) to a resonant autoionization state at 110,296.0 cm^{-1} (Kramida et al. 2014). The ions formed in the interaction region are accelerated by the ion imaging optics down a 72.5 cm flight tube, where they strike a dual microchannel plate (MCP) detector (active diameter = 7.5 cm) that converts them to electrons. A high-voltage pulse is applied to the front MCP at the expected arrival time of N^+ ions to select them from other ions for detection. The optical image resulting from the electron impact on the phosphor screen is recorded using a CCD camera.

3. AB INITIO CALCULATIONS OF POTENTIAL ENERGY CURVES OF UNGERADE N_2 STATES

Single-photon VUV excitation from the $N_2(X^1\Sigma_g^+)$ ground - state can only populate the ungerade states. Many of these ungerade states can be coupled by spin–orbit or vibronic interactions. Hence, only the ungerade states of N_2 are calculated and presented. Because of the potential diffuse nature of the excited states, their wavefunctions were calculated using a large basis set composed by the aug-cc-pVQZ quality, which is augmented by 3*s* and 2*p* diffuse Gaussian-type orbitals (GTOs; Dunning 1989; Kendall et al. 1992; Woon & Dunning 1995). In addition, the expected high density of the electronic states in this energy range should lead to the mixing of their electronic wavefunctions. Therefore, a multiconfigurational approach is adopted where the electronic computations were carried out using the Complete Active Space Self Consistent Field (CASSCF; Knowles & Werner 1985; Werner & Knowles 1985) approach followed by the internally contracted Multi Reference Configuration Interaction (MRCI; Knowles & Werner 1988; Werner & Knowles 1988) technique as implemented in MOLPRO (Werner et al. 2012). We followed the procedure established in Spelsberg & Meyer (2001), Ndome et al. (2008), and Hochlaf et al. (2010a, 2010b). Briefly, the CASSCF active space is constructed by the valence molecular orbitals (MOs) of N_2 increased by one s_g and one p_g MOs. This allows better relaxation of the wavefunctions of the N_2 electronic states whose configurations differ in their *s* and *p* orbital occupations as those of interest at present. In MRCI, all CASSCF configurations were taken into account as reference. Finally, the CASSCF wavefunctions were used to evaluate the spin–orbit matrix elements. These spin–orbit computations were performed in Cartesian coordinates, where the CASSCF wavefunctions were used as the multielectron basis for the two-step spin–orbit coupling calculation (Llusar et al. 1996; Zeng et al. 2011) through the Breit–Pauli Hamiltonian (Berning et al. 2000) as implemented in MOLPRO.

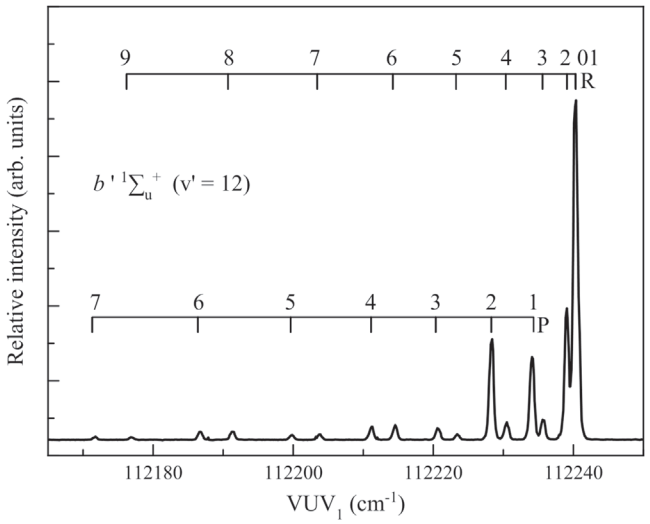

Figure 1. Photofragment excitation (PHOFEX) spectrum of N(^{4}S) atoms formed in the photodissociation of $N_2(b'^1\Sigma_u^+;\ v' = 12, J')$ in the VUV_1 region of 112,165–112,250 cm^{-1}. The P(J″) and R(J″) rotational transition lines from the N_2 ($X^1\Sigma_g^+;\ v'' = 0, J''$) state are denoted. The bandwidth of the VUV_1 laser used is 0.4 cm^{-1} (FWHM), which is narrower than the observed rotational bandwidth of 0.5–1.0 cm^{-1} (FWHM), indicative of the Doppler effect due to the large recoil velocity of N atoms formed in the photodissociation process.

4. RESULTS AND DISCUSSION

4.1. Photofragment Excitation Spectrum

Figure 1(a) is an example of the photofragment excitation (PHOFEX) spectrum of N(^{4}S) atoms obtained by tuning the VUV_1 energy [$h\nu(VUV_1)$] in the range of 112,165–112,250 cm^{-1} to excite the $N_2(b'^1\Sigma_u^+;\ v' = 12) \leftarrow N_2(X^1\Sigma_g^+;\ v'' = 0)$ band, while setting the VUV_2 laser output to ionize the N(^{4}S) atomic photofragments. The rotational line positions agree with known line positions for this band, with deviations in the range of 0.5–1.0 cm^{-1} (Dressler 1969; Roncin et al. 1998). The measurements and reliable assignments of a PHOFEX spectrum are an important step in ensuring the correct identification of selected excited predissociative rovibronic states of N_2. The line widths of the individual rotational lines in Figure 1 are equal to 0.82 cm^{-1} (FWHM), which should be mainly due to the Doppler effect caused by the large recoil velocity of N atoms formed in the photodissociation process. The contribution of the power broadening effect to the observed experimental line width is expected to be unimportant because the VUV sum-frequency output is low (10–100 μJ/pulse) and unfocused.

4.2. State-selected Branching Ratios for State-correlated Photoproducts

Figure 2(a) shows the time-slice VMI-PI image of N(^{4}S) recorded by fixing the $h\nu(VUV_1)$ at the R(2) rotational transition (112,239.0 cm^{-1}) of the $N_2(b'^1\Sigma_u^+;\ v' = 12)$ vibrational band and ionizing the N(^{4}S) atom 15 ns later with the $h\nu(VUV_2)$. There are two well-separated rings in the image, indicating the formation of two N(^{4}S) product channels in the photodissociation of $N_2(b'^1\Sigma_u^+;\ v' = 12, J'=3)$. By measuring the radii of these circles and converting them to energies using the energy calibration of the VMI-PI apparatus, the center-of-mass kinetic energies (E_{cm}) are determined for the two N_2 photoproduct channels using Equation (5), which is derived based on the conservation of linear momentum and energy:

$$E_{cm} = E_{TKER} = h\nu\,(VUV_1) - D_0(N_2) - E\,(\text{N atoms}). \quad (5)$$

Here E_{cm} is referred to as the total kinetic energy release (E_{TKER}), $D_0(N_2) = 78{,}714\ cm^{-1}$ is the 0 K bond dissociation energy, and E(N atoms) is the internal electronic energies of the two photoproduct N atoms. The E(N atoms) = 0, 19,224, 28,839, and 38,448 cm^{-1} for the formation of N(^{4}S) + N(^{4}S), N(^{4}S) + N(^{2}D), N(^{4}S) + N(^{2}P), and N(^{2}D) + N(^{2}D) channels, respectively (Kramida et al. 2014). The E_{TKER} spectrum converted from the VMI-PI image of Figure 2(a) is shown in Figure 2(b), where the two peaks resolved in the E_{TKER} spectrum are assigned to the formation of the N(^{4}S) + N(^{2}D) and N(^{4}S) + N(^{2}P) channels. The integrated areas of these two peaks yield a branching ratio N(^{4}S) + N(^{2}D):N(^{4}S) + N(^{2}P) of 0.76 ± 0.03:0.24 ± 0.04. Similar procedures are used to determine the branching ratios for all of the upper energy levels of N_2 that can be excited with the VUV_1 laser in the energy range of 100,808–122,159 cm^{-1}, and the results are collected in Tables 1–5. The error bars presented are simply the statistical uncertainties (1σ) from three to four independent measurements and thus should only represent the lower limits of the real uncertainties. Those values without error bars are from single measurements except for unity and zero branching

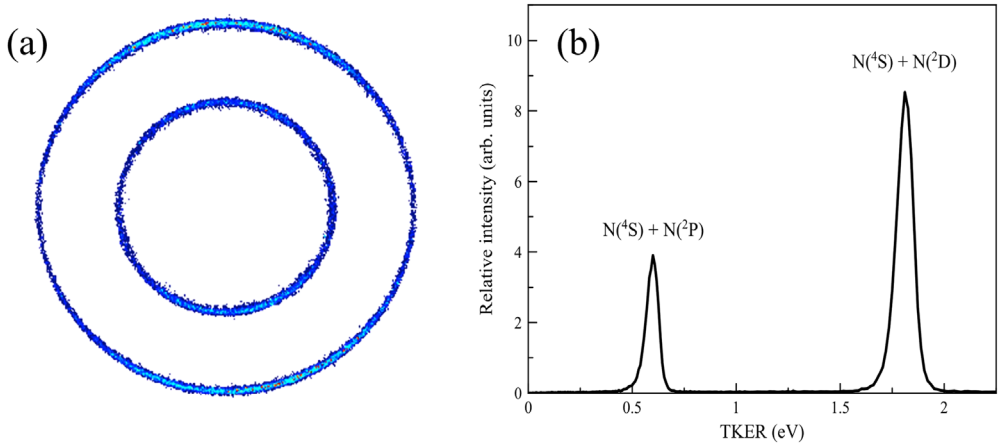

Figure 2. (a) Time-slice VMI-PI image of N(^{4}S) produced by photodissociation of N_2 with $h\nu(VUV_1)$ set at the R(2) rotational line (112,239.0 cm^{-1}) of N_2 ($b'^1\Sigma_u^+$, $v' = 12$) band. (b) TKER spectrum converted from the VMI-PI image shown in (a). The assignment of the N(^{4}S) + N(^{2}D) and N(^{4}S) + N(^{2}P) channels is also marked in (b).

Table 1
Product Branching Ratios for the N(^{4}S) + N(^{2}D), N(^{4}S) + N(^{2}P), and N(^{2}D) + N(^{2}D) Channels from Excitation to the N_2 ($b^1\Pi_u$; $v' = 0$–23, J') Valence States in N_2 Photodissociation

Term	v'	J''	VUV_1 (cm^{-1})	N (^{4}S) + N(^{2}D)	N (^{4}S) + N(^{2}P)	N(^{2}D) + N(^{2}D)
$b(^1\Pi_u)$	$v' = 0$	P(2)	100807.7	1.000	0.000	0.000
		Q(2)	100813.5	1.000	0.000	0.000
		Q(1)	100815.6	1.000	0.000	0.000
		R(0)	100819.7	1.000	0.000	0.000
		R(1)	100821.5	1.000	0.000	0.000
		R(2)	100822.2	1.000	0.000	0.000
$b(^1\Pi_u)$	$v' = 1$	P(2)	101442.3	1.000	0.000	0.000
		Q(2)	101448.0	1.000	0.000	0.000
		Q(1)	101450.3	1.000	0.000	0.000
		R(0)	101454.2	1.000	0.000	0.000
		R(1)	101456.0	1.000	0.000	0.000
$b(^1\Pi_u)$	$v' = 2$	Q(2)	102148.2	1.000	0.000	0.000
		Q(1)	102150.7	1.000	0.000	0.000
		R(0)	102154.7	1.000	0.000	0.000
		R(1)	102156.2	1.000	0.000	0.000
$b(^1\Pi_u)$	$v' = 3$	R(0)	102864.8	1.000	0.000	0.000
$b(^1\Pi_u)$	$v' = 4$	P(2)	103539.6	1.000	0.000	0.000
		Q(2)	103545.4	1.000	0.000	0.000
		Q(1)	103547.6	1.000	0.000	0.000
		R(0)	103551.6	1.000	0.000	0.000
		R(1)	103553.4	1.000	0.000	0.000
$b(^1\Pi_u)$	$v' = 5$	P(2)	104690.8	1.000	0.000	0.000
		Q(2)	104696.4	1.000	0.000	0.000
		Q(1)	104698.7	1.000	0.000	0.000
		R(0)	104702.7	1.000	0.000	0.000
		R(1)	104704.6	1.000	0.000	0.000
		R(2)	104705.1	1.000	0.000	0.000
$b(^1\Pi_u)$	$v' = 6$	P(2)	105336.6	1.000	0.000	0.000
		Q(2)	105342.1	1.000	0.000	0.000
		Q(1)	105344.6	1.000	0.000	0.000
		R(0)	105348.6	1.000	0.000	0.000
		R(1)	105350.0	1.000	0.000	0.000
$b(^1\Pi_u)$	$v' = 7$	P(2)	106100.2	1.000	0.000	0.000
		Q(2)	106105.6	1.000	0.000	0.000
		Q(1)	106108.3	1.000	0.000	0.000
		R(0)	106112.3	1.000	0.000	0.000
		R(1)	106113.6	1.000	0.000	0.000
$b(^1\Pi_u)$	$v' = 8$	P(2)	106923.7	1.000	0.000	0.000
		Q(2)	106928.9	1.000	0.000	0.000
		Q(1)	106931.6	1.000	0.000	0.000
		R(0)	106935.6	1.000	0.000	0.000
		R(1)	106937.0	1.000	0.000	0.000
$b(^1\Pi_u)$	$v' = 9$	P(2)	107642.3	1.000	0.000	0.000
		Q(2)	107647.8	1.000	0.000	0.000
		Q(1)	107650.3	1.000	0.000	0.000
		R(0)	107654.3	1.000	0.000	0.000
		R(1)	107655.8	1.000	0.000	0.000
$b(^1\Pi_u)$	$v' = 10$	P(2)	108362.4	1.000	0.000	0.000
		Q(2)	108367.3	1.000	0.000	0.000
		Q(1)	108370.3	1.000	0.000	0.000
		R(0)	108374.4	1.000	0.000	0.000
		R(1)	108375.1	1.000	0.000	0.000
$b(^1\Pi_u)$	$v' = 11$	Q(2)	109115.1	1.000	0.000	0.000
		Q(1)	109119.0	1.000	0.000	0.000
		R(3)	109120.0	1.000	0.000	0.000
		R (0,1,2)	109122.8	1.000	0.000	0.000
$b(^1\Pi_u)$	$v' = 12$	Q(2)	109826.1	0.999 ± 0.001	0.002 ± 0.001	0.000
		Q(1)	109829.4	0.999[a]	0.001[a]	0.000
		R(0)	109833.5	0.994 ± 0.005	0.006 ± 0.005	0.000
$b(^1\Pi_u)$	$v' = 13$	Q(1)	110527.3	1.000	0.000	0.000
		R(0)	110530.8	1.000	0.000	0.000
$b(^1\Pi_u)$	$v' = 14$	P(2)	111199.9	1.000	0.000	0.000

Table 1
(Continued)

Term	v'	J''	VUV_1 (cm^{-1})	N (^4S) + N(^2D)	N (^4S) + N(^2P)	N(^2D) + N(^2D)
		Q(2)	111204.3	1.000	0.000	0.000
		Q(1)	111207.9	1.000	0.000	0.000
		R(2)	111210.9	1.000	0.000	0.000
		R(0,1)	111211.9	1.000	0.000	0.000
$b(^1\Pi_u)$	$v' = 15$	Q(2)	111866.6	0.980 ± 0.005	0.020 ± 0.005	0.000
		Q(1)	111870.4	0.978 ± 0.013	0.022 ± 0.005	0.000
		R(2)	111873.1	0.986 ± 0.002	0.014 ± 0.002	0.000
		R(0,1)	111874.4	0.982 ± 0.007	0.018 ± 0.007	0.000
$b(^1\Pi_u)$	$v' = 16$	Q(2)	112502.8	1.000	0.000	0.000
		Q(1)	112506.6	1.000	0.000	0.000
		R(2)	112509.2	1.000	0.000	0.000
		R(0,1)	112510.6	1.000	0.000	0.000
$b(^1\Pi_u)$	$v' = 17$	Q(2)	113121.4	0.118 ± 0.006	0.882 ± 0.006	0.000
		Q(1)	113125.4	0.136 ± 0.006	0.864 ± 0.006	0.000
		R(2)	113127.3	0.130 ± 0.007	0.870 ± 0.007	0.000
		R(0,1)	113129.3	0.119 ± 0.009	0.881 ± 0.009	0.000
$b(^1\Pi_u)$	$v' = 18$	Q(2)	113701.1	0.207 ± 0.020	0.793 ± 0.020	0.000
		Q(1)	113705.3	0.246 ± 0.012	0.754 ± 0.012	0.000
		R(2)	113707.1	0.250 ± 0.006	0.750 ± 0.006	0.000
		R(0,1)	113709.3	0.214 ± 0.009	0.786 ± 0.009	0.000
$b(^1\Pi_u)$	$v' = 19$	R(0,1)	114256.7	0.896 ± 0.023	0.104 ± 0.023	0.000
$b(^1\Pi_u)$	$v' = 22$	R(0)	115664.7	0.955 ± 0.003	0.045 ± 0.003	0.000
$b(^1\Pi_u)$	$v' = 23$	Q(1)	116026.6	1.000 ± 0.005	0.000 ± 0.005	0.000
		R(0)	116030.5	0.983 ± 0.005	0.017 ± 0.005	0.000

Note.
[a] Value determined by one ion image; the uncertainty is estimated to be 1%–3% based on the counting statistics.

ratios. Considering that the ion counts collected for each ion image for the branching ratio determination are more than 10,000 and the detection method used here is very clean, we have assigned the uncertainty of 1%–3% for those branching ratios from single measurements. The electronic states that are populated by single-photon VUV excitation are all singlet states except for the triplet $N_2(C^3\Pi_u;\ v' = 16,\ J')$ states that have been previously observed in VUV absorption studies (Carroll & Mulliken 1965; Lewis et al. 2008a).

In the above example, where N_2 is excited to the $N_2(b'^1\Sigma_u^+;\ v' = 12,\ J'=3)$ state at 112,239 cm^{-1}, the spin-allowed N(^4S) + N(^4S) ground-state channel was not observed, i.e., the branching ratio for Reaction (1) is zero. The same result is found for all of the levels excited throughout the 100,808–122,159 cm^{-1} range of the present study. This is in agreement with the earlier studies using the fast-beam method over a narrower energy range of 110,175–112,917 cm^{-1} (Helm & Cosby 1989; Walter et al. 1993, 1994). This observation proves that internal conversion to the excited vibrational levels of the ground electronic state is not competitive with intersystem crossing at any of the energies in the present studies. Furthermore, it provides evidence that photoexcited N_2 molecules cannot undergo spin–orbit allowed conversion to reach electronic states, which correlate to the N(^4S) + N(^4S) ground-state channel.

The branching ratios of Tables 1–5 cover the $h\nu(VUV_1)$ range of 100,808–122,159 cm^{-1}. Tables 1 and 2 list the branching ratios for the product channels, N(^4S) + N(^2D), N(^4S) + N(^2P), and N(^2D) + N(^2D), via excitation to the valence N_2 states, $(b^1\Pi_u;\ v' = 0–23)$, and the Rydberg N_2 states, $(c_3{}^1\Pi_u;\ v' = 0,\ 1,\ 3)$, $(o_3{}^1\Pi_u;\ v' = 0,\ 2–4)$, $(c_4{}^1\Pi_u;\ v' = 0–2)$, $(c_5{}^1\Pi_u;\ v' = 0)$, $(c_6{}^1\Pi_u;\ v' = 0)$, and $(o_4^1\Pi_u;\ v' = 0)$, respectively. The branching ratios for the product channels from the valence N_2 states, $(b'^1\Sigma_u^+;\ v' = 1–28)$, and the Rydberg N_2 states, $(c_4'^1\Sigma_u^+;\ v' = 0–8)$, $(c_5'^1\Sigma_u^+;\ v' = 0–2)$, and $(c_6'^1\Sigma_u^+;\ v' = 0)$, are given in Tables 3 and 4, respectively. Branching ratios produced via the valence N_2 states, $(C^3\Pi_u;\ v' = 16,\ J')$, and the Rydberg N_2(4f and 5f) complex states, $[X^+(0)4f;\ v' = 0–1,\ J']$, $[X^+(1)4f;\ v' = 0–1,\ J']$, and $[X^+(0)5f;\ v' = 0–1,\ J']$, are listed in Table 5. The branching ratios given in parentheses in the tables were reported previously by the fast ion beam study. Generally, the branching ratios obtained in the present measurements have smaller error limits than those reported previously. Taking into account experimental uncertainties, the branching ratios obtained here and those reported in the fast-beam experiment (Helm & Cosby 1989; Walter et al. 1993, 1994; Cosby & Walter 1996) are in reasonable agreement.

To better examine the trends of the branching ratios listed in Tables 1–4, they are plotted in Figures 3(a)–(d) for the N(^4S) + N(^2D) (blue curve), N(^4S) + N(^2P) (red curve), and N(^2D) + N(^2D) (green curve) channels as a function of $h\nu(VUV_1)$. The energetic thresholds for the formation of the N(^4S) + N(^2P) and N(^2D) + N(^2D) channels are also marked in these figures by downward-pointing red and green arrows, respectively. The energetic threshold of 97,938 cm^{-1} for the N(^4S) + N(^2D) channel is well below the $h\nu(VUV_1)$ range of the present study and is not marked in the figures. The valence N_2 states $(b^1\Pi_u;\ v' \leqslant 23)$ that can be populated by single-photon VUV excitation are below the energetic threshold for the N(^2D) + N(^2D) channel, so they are not observed in Figure 3(a).

The comparison of photoproduct branching ratio curves of Figures 3(a)–(d) indicates that the branching ratios for Reactions (2)–(4) depend not only on $h\nu(VUV_1)$ but also on

Table 2
Product Branching Ratios for the $N(^4S) + N(^2D)$, $N(^4S) + N(^2P)$, and $N(^2D) + N(^2D)$ Channels from Excitation to the N_2 (c_{3-6} and o_3 $^1\Pi_u$; v', J'), $(A^+(0)3d\sigma^1\Pi_u; v', J')$, and $(X^+(1)5p\pi^1\Pi_u; v', J')$ Rydberg States in N_2 Photodissociation

Term	v'	J''	VUV_1 (cm^{-1})	$N(^4S) + N(^2D)$	$N(^4S) + N(^2P)$	$N(^2D) + N(^2D)$
$c_3(^1\Pi_u)$	$v' = 0$	P(2)	104129.4	1.000	0.000	0.000
		Q(2)	104135.5	1.000	0.000	0.000
		Q(1)	104137.4	1.000	0.000	0.000
		R(0)	104141.4	1.000	0.000	0.000
		R(1)	104143.3	1.000	0.000	0.000
		R(2)	104144.2	1.000	0.000	0.000
$o_3(^1\Pi_u)$	$v' = 0$	R(0)	105686.3	1.000	0.000	0.000
$c_3(^1\Pi_u)$	$v' = 1$	P(2)	106519.5	1.000	0.000	0.000
		Q(2)	106526.3	1.000	0.000	0.000
		Q(1)	106527.5	1.000	0.000	0.000
		R(0)	106531.5	1.000	0.000	0.000
		R(1)	106534.3	1.000	0.000	0.000
		R(2)	106536.6	1.000	0.000	0.000
$o_3(^1\Pi_u)$	$v' = 1$	Q(2)	107627.0	1.000	0.000	0.000
		R(0)	107632.6	1.000	0.000	0.000
$o_3(^1\Pi_u)$	$v' = 2$	Q(2)	109559.9	1.000	0.000	0.000
		Q(1)	109561.0	1.000	0.000	0.000
		R(0)	109564.9	1.000	0.000	0.000
		R(1)	109567.8	1.000	0.000	0.000
		R(2)	109570.1	1.000	0.000	0.000
$c_3(^1\Pi_u)$	$v' = 3$	Q(1)	110795.4	1.000	0.000	0.000
		R(0)	110799.8	1.000 (0.96)[a]	0.000 (0.04)[a]	0.000
$o_3(^1\Pi_u)$	$v' = 3$	P(2)	111438.9	1.000	0.000	0.000
		Q(4)	111441.5	1.000	0.000	0.000
		Q(3)	111444.1	1.000	0.000	0.000
		Q(2)	111445.6	1.000	0.000	0.000
		Q(1)	111446.8	1.000	0.000	0.000
		R(0)	111450.8	1.000	0.000	0.000
		R(1)	111453.7	1.000	0.000	0.000
		R(2)	111455.9	1.000	0.000	0.000
		R(3)	111457.5	1.000 (>0.99)[a]	0.000 (<0.01)[a]	0.000
		R(4)	111458.5	1.000	0.000	0.000
$o_3(^1\Pi_u)$	$v' = 4$	Q(2)	113305.7	1.000	0.000	0.000
		Q(1)	113306.8	1.000	0.000	0.000
		R(0)	113310.9	1.000	0.000	0.000
		R(1)	113313.6	1.000	0.000	0.000
		R(2)	113316.0	1.000	0.000	0.000
$c_3(^1\Pi_u)$	$v' = 5$	Q(2)	114830.3	0.979 ± 0.004	0.021 ± 0.004	0.000
		Q(1)	114831.4	0.978 ± 0.009	0.022 ± 0.009	0.000
$o_3(^1\Pi_u)$	$v' = 5$	Q(2)	115253.0	0.864[b]	0.136[b]	0.000
		Q(1)	115256.9	0.863[b]	0.137[b]	0.000
		R(0,2)	115260.8	0.866 ± 0.007	0.134 ± 0.007	0.000
$c_4(^1\Pi_u)$	$v' = 0$	Q(1)	115565.4	1.000	0.000	0.000
$c_4(^1\Pi_u)$	$v' = 0$	R(0)	115569.4	0.984 ± 0.021 (0.938 ± 0.004)[c]	0.017 ± 0.021 (0.062 ± 0.004)[c]	0.000
		R(1)	115573.1	0.917 ± 0.013 (0.873 ± 0.006)[c]	0.083 ± 0.013 (0.127 ± 0.006)[c]	0.000
		R(2)	115576.6	0.841 ± 0.010 (0.79 ± 0.02)[c]	0.160 ± 0.010 (0.21 ± 0.02)[c]	0.000
$c_4(^1\Pi_u)$	$v' = 1$	R(0)	117750.8	0.042 ± 0.013	0.000	0.958 ± 0.035
$c_5(^1\Pi_u)$	$v' = 0$	Q(1)	119739.1	0.862 ± 0.034	0.000	0.138 ± 0.034
		R(0)	119743.0	0.862 ± 0.026	0.000	0.138 ± 0.026
		R(1)	119746.4	0.847 ± 0.029	0.000	0.153 ± 0.029
		R(2)	119749.7	0.840 ± 0.028	0.000	0.160 ± 0.028
$c_4(^1\Pi_u)$	$v' = 2$	Q(1)	119890.0	0.000	0.000	1.000
		R(0)	119894.2	0.000	0.000	1.000
$A^+(0)3d\sigma^1\Pi_u$	$v' = 0$	Q(2)	121118.6	0.870 ± 0.008	0.000	0.130 ± 0.008
		Q(1)	121119.6	0.862 ± 0.000	0.000	0.138 ± 0.000
		R(0)	121123.7	0.847 ± 0.007	0.000	0.153 ± 0.007
		R(1)	121126.1	0.862 ± 0.007	0.000	0.138 ± 0.007
$c_6(^1\Pi_u)$	$v' = 0$	R(0)	121774.1	0.822 ± 0.007	0.000	0.178 ± 0.002
$X^+(1)\ 5p\pi^1\Pi_u$	$v' = 1$	R(0)	121924.6	0.455 ± 0.052	0.000	0.545 ± 0.052
$A^+(0)3d\delta^1\Pi_u$	$v' = 0$	R(0)	122159.1	0.884 ± 0.005	0.000	0.116 ± 0.005

Notes.
[a] Reported by Walter et al. (1993).
[b] Value determined by one ion image; the uncertainty is estimated to be 1%–3% based on the counting statistics.
[c] Reported by Cosby & Walter (1996).

Table 3
Product Branching Ratios for the $N(^4S) + N(^2D)$, $N(^4S) + N(^2P)$, and $N(^2D) + N(^2D)$ Channels from Excitation to the $N_2(b'^1\Sigma_u^+; v' = 1–28, J')$ Valence States in N_2 Photodissociation

Term	v'	J''	VUV$_1$ (cm^{-1})	$N(^4S)+N(^2D)$	$N(^4S)+N(^2P)$	$N(^2D)+N(^2D)$
$b'(^1\Sigma_u^+)$	$v' = 1$	R(0)	104420.4	1.000	0.000	0.000
$b'(^1\Sigma_u^+)$	$v' = 2$	R(0)	105153.3	1.000	0.000	0.000
$b'(^1\Sigma_u^+)$	$v' = 3$	P(2)	105859.7	1.000	0.000	0.000
		P(1)	105865.3	1.000	0.000	0.000
		R(0)	105871.6	1.000	0.000	0.000
$b'(^1\Sigma_u^+)$	$v' = 4$	P(2)	106637.2	1.000	0.000	0.000
		P(1)	106642.7	1.000	0.000	0.000
		R(0)	106649.2	1.000	0.000	0.000
		R(1)	106650.3	1.000	0.000	0.000
$b'(^1\Sigma_u^+)$	$v' = 5$	P(2)	107316.5	1.000	0.000	0.000
		P(1)	107322.2	1.000	0.000	0.000
		R(0)	107328.4	1.000	0.000	0.000
$b'(^1\Sigma_u^+)$	$v' = 6$	P(3)	107982.1	1.000	0.000	0.000
		P(2)	107989.3	1.000	0.000	0.000
		P(1)	107994.7	1.000	0.000	0.000
		R(3)	107999.1	1.000	0.000	0.000
		R(0,2)	108001.2	1.000	0.000	0.000
		R(1)	108002.0	1.000	0.000	0.000
$b'(^1\Sigma_u^+)$	$v' = 7$	P(2)	108943.1	1.000	0.000	0.000
		P(1)	108948.2	1.000	0.000	0.000
		R(0)	108954.9	1.000	0.000	0.000
		R(1)	108956.5	1.000	0.000	0.000
$b'(^1\Sigma_u^+)$	$v' = 8$	P(2)	109534.2	0.997[a]	0.003[a]	0.000
		P(1)	109539.8	0.997[a]	0.003[a]	0.000
		R(2)	109545.6	0.993[a]	0.007[a]	0.000
		R(0)	109546.2	0.997 ± 0.002	0.003 ± 0.002	0.000
		R(1)	109546.4	0.988[a]	0.012[a]	0.000
$b'(^1\Sigma_u^+)$	$v' = 9$	P(2)	110187.2	0.639 ± 0.007	0.361 ± 0.007	0.000
		P(1)	110192.7	0.618 ± 0.017	0.382 ± 0.017	0.000
		R(2)	110198.4	0.672 ± 0.019 (0.96)[b]	0.328 ± 0.019 (0.04)[b]	0.000
		R(0)	110199.0	0.694 ± 0.004	0.307 ± 0.004	0.000
		R(1)	110199.5	0.674 ± 0.007	0.326 ± 0.007	0.000
$b'(^1\Sigma_u^+)$	$v' = 10$	P(2)	110932.8	0.987 ± 0.001	0.013 ± 0.001	0.000
		P(1)	110938.2	0.986 ± 0.004	0.015 ± 0.004	0.000
		R(2)	110944.8	0.988 ± 0.003 (1.00 ± 0.03)[c]	0.012 ± 0.003 (0.00 ± 0.03)[c]	0.000
		R(0)	110945.3	0.979[a](0.98)[b]	0.021[a](0.02)[b]	0.000
		R(1)	110945.9	0.987 ± 0.005(0.99)[b]	0.013 ± 0.005 (0.01)[b]	0.000
$b'(^1\Sigma_u^+)$	$v' = 11$	P(3)	111563.6	0.986[a]	0.014[a]	0.000
		P(2)	111571.1	0.994 ± 0.002	0.006 ± 0.002	0.000
$b'(^1\Sigma_u^+)$	$v' = 11$	P(1)	111576.9	0.992 ± 0.001 (0.97)[b]	0.008 ± 0.001 (0.03)[b]	0.000
		R(3)	111578.9	0.977[a] (0.99 ± 0.05)[c]	0.023[a] (0.01 ± 0.05)[c]	0.000
		R(2)	111582.1	0.987[a] (1.00 ± 0.05)[c]	0.013[a] (0.00 ± 0.05)[c]	0.000
		R(0,1)	111583.0	0.990 ± 0.006 (0.97 ± 0.05)[c]	0.010 ± 0.006 (0.03 ± 0.05)[c]	0.000
$b'(^1\Sigma_u^+)$	$v' = 12$	P(6)	112186.7	0.687[a] (0.78 ± 0.02)[c]	0.313[a] (0.22 ± 0.02)[c]	0.000
		R(8)	112191.5	0.702[a](0.72)[b]	0.298[a](0.28)[b]	0.000
		P(5)	112199.8	0.734[a](0.73 ± 0.04)[c]	0.266[a](0.27 ± 0.04)[c]	0.000
		R(7)	112203.9	0.619[a](0.77)[b]	0.381[a](0.23)[b]	0.000
		P(4)	112211.3	0.764 ± 0.022 (0.79 ± 0.03)[c]	0.236 ± 0.022 (0.21 ± 0.03)[c]	0.000
		R(6)	112214.5	0.761 ± 0.079 (0.76)[b]	0.239 ± 0.079 (0.24)[b]	0.000
		P(3)	112220.7	0.773 ± 0.016 (0.78 ± 0.07)[c]	0.227 ± 0.016 (0.22 ± 0.07)[c]	0.000
		R(5)	112223.6	0.753 ± 0.072 (0.80)[b]	0.247 ± 0.072 (0.2)[b]	0.000
		P(2)	112228.6	0.771 ± 0.027	0.229 ± 0.027	0.000
		R(4)	112230.5	0.758 ± 0.023 (0.73)[b]	0.242 ± 0.023 (0.27)[b]	0.000
		P(1)	112234.1	0.759 ± 0.030	0.241 ± 0.030	0.000
		R(3)	112235.6	0.771 ± 0.023 (0.79)[b]	0.229 ± 0.023 (0.21)[b]	0.000
		R(2)	112239.0	0.761 ± 0.028 (0.86)[b]	0.239 ± 0.028 (0.14)[b]	0.000
		R(0,1)	112240.4	0.784 ± 0.014 (0.78 ± 0.07)[c]	0.210 ± 0.015 (0.22 ± 0.07)[c]	0.000
$b'(^1\Sigma_u^+)$	$v' = 13$	P(2)	112898.4	0.216 ± 0.023 (0.248 ± 0.036)[c]	0.784 ± 0.023 (0.752 ± 0.036)[c]	0.000
		P(1)	112904.0	0.220 ± 0.016 (0.22)[b]	0.780 ± 0.016 (0.78)[b]	0.000
		R(0,2)	112910.3	0.182 ± 0.016	0.818 ± 0.016	0.000
		R(1)	112911.1	0.205 ± 0.002 (0.255 ± 0.03)[c]	0.795 ± 0.002 (0.745 ± 0.03)[c]	0.000
$b'(^1\Sigma_u^+)$	$v' = 14$	P(2)	113530.6	0.054 ± 0.014	0.946 ± 0.014	0.000
		P(1)	113536.6	0.053 ± 0.014	0.947 ± 0.014	0.000

Table 3
(Continued)

Term	v'	J''	VUV_1 (cm^{-1})	$N(^4S)+N(^2D)$	$N(^4S)+N(^2P)$	$N(^2D)+N(^2D)$
		R(2)	113541.0	0.047 ± 0.016	0.953 ± 0.016	0.000
		R(0,1)	113542.6	0.057 ± 0.019	0.943 ± 0.019	0.000
$b'(^1\Sigma_u^+)$	$v' = 15$	P(2)	114159.9	0.156 ± 0.008 (0.164 ± 0.07)[c]	0.844 ± 0.008 (0.836 ± 0.07)[c]	0.000
		P(1)	114165.7	0.145 ± 0.008 (0.116 ± 0.01)[c]	0.855 ± 0.008 (0.884 ± 0.01)[c]	0.000
		R(2)	114170.3	0.166 ± 0.010 (0.159 ± 0.049)[c]	0.834 ± 0.010 (0.841 ± 0.049)[c]	0.000
		R(0,1)	114171.9	0.163 ± 0.010	0.838 ± 0.010	0.000
$b'(^1\Sigma_u^+)$	$v' = 16$	P(4)	114730.5	0.977 ± 0.003 (0.985 ± 0.004)[c]	0.023 ± 0.003 (0.015 ± 0.004)[c]	0.000
		P(3)	114738.4	0.982 ± 0.005 (0.982 ± 0.013)[c]	0.018 ± 0.005 (0.018 ± 0.013)[c]	0.000
		P(2)	114744.8	0.990 ± 0.001 (0.998 ± 0.001)[c]	0.010 ± 0.001 (0.002 ± 0.001)[c]	0.000
		R(5)	114748.6	0.980 ± 0.002 (0.968 ± 0.008)[c]	0.020 ± 0.002 (0.032 ± 0.008)[c]	0.000
		P(1)	114749.9	0.993 ± 0.001 (0.907 ± 0.036)[c]	0.007 ± 0.001 (0.093 ± 0.036)[c]	0.000
		R(4)	114753.5	0.968 ± 0.003 (0.976 ± 0.004)[c]	0.032 ± 0.003 (0.024 ± 0.004)[c]	0.000
		R(0)	114756.7	0.987 ± 0.001 (0.998 ± 0.001)[c]	0.013 ± 0.001 (0.002 ± 0.001)[c]	0.000
		R(0,2)	114758.2	0.984 ± 0.002	0.016 ± 0.002	0.000
$b'(^1\Sigma_u^+)$	$v' = 17$	P(2)	115359.5	0.535 ± 0.013 (0.347 ± 0.112)[c]	0.465 ± 0.013 (0.653 ± 0.112)[c]	0.000
		P(1)	115365.2	0.540 ± 0.007 (0.465 ± 0.152)[c]	0.460 ± 0.007 (0.535 ± 0.152)[c]	0.000
		R(0)	115371.4	0.532 ± 0.007 (0.347 ± 0.112)[c]	0.468 ± 0.007 (0.653 ± 0.112)[c]	0.000
$b'(^1\Sigma_u^+)$	$v' = 18$	P(2)	116197.2	0.241 ± 0.006	0.759 ± 0.006	0.000
		P(1)	116202.5	0.235 ± 0.003	0.765 ± 0.003	0.000
		R(0)	116209.1	0.207 ± 0.028	0.793 ± 0.028	0.000
		R(0,2)	116210.2	0.222 ± 0.011	0.778 ± 0.011	0.000
$b'(^1\Sigma_u^+)$	$v' = 19$	P(2)	116672.7	0.054 ± 0.007	0.946 ± 0.007	0.000
		P(1)	116678.4	0.050 ± 0.005	0.950 ± 0.005	0.000
		R(2)	116683.6	0.064 ± 0.001	0.936 ± 0.001	0.000
		R(0,1)	116684.7	0.053 ± 0.004	0.947 ± 0.004	0.000
$b'(^1\Sigma_u^+)$	$v' = 20$	R(0,1)	117206.9	0.054 ± 0.006	0.925 ± 0.005	0.021 ± 0.007
$b'(^1\Sigma_u^+)$	$v' = 21$	R(0)	117684.2	0.400 ± 0.043	0.156 ± 0.030	0.444 ± 0.028
$b'(^1\Sigma_u^+)$	$v' = 22$	P(1)	118481.1	0.235 ± 0.053	0.000	0.765 ± 0.053
		R(0,1)	118487.4	0.332 ± 0.091	0.333 ± 0.001	0.635 ± 0.078
$b'(^1\Sigma_u^+)$	$v' = 23$	R(0,1)	118970.0	0.257 ± 0.087	0.023 ± 0.001	0.710 ± 0.089
$b'(^1\Sigma_u^+)$	$v' = 24$	R(0,1)	119431.7	0.426 ± 0.076	0.051 ± 0.001	0.523 ± 0.077
$b'(^1\Sigma_u^+)$	$v' = 25$	R(0,1)	119837.0	0.460 ± 0.019	0.000	0.540 ± 0.019
$b'(^1\Sigma_u^+)$	$v' = 26$	R(0)	120586.2	0.342 ± 0.025	0.000	0.658 ± 0.025
$b'(^1\Sigma_u^+)$	$v' = 27$	R(0)	121037.2	0.327 ± 0.015	0.000	0.673 ± 0.015
$b'(^1\Sigma_u^+)$	$v' = 28$	R(0)	121453.5	0.000	0.000	1.000

Notes.
[a] Value determined by one ion image; the uncertainty is estimated to be 1%–3% based on the counting statistics.
[b] Reported by Walter et al. (1993).
[c] Reported by Cosby & Walter (1996).

the predissociative rovibronic states of N_2. Although Figures 3(a)–(d) cover the common $h\nu(VUV_1)$ range, the branching ratio curves associated with the respective four sets of predissociative N_2 states, i.e., valence and Rydberg $N_2(\Pi_u;\ v',\ J')$ and $N_2(^1\Sigma_u^+;\ v',\ J')$ states, are distinctly different. The different predissociative N_2 states with similar internal energies are found to follow different dissociation pathways, indicating that they are not statistical. Therefore, the formation of a selected photoproduct can be controlled by exciting a particular quantum state.

For N_2 photodissociation via the valence and Rydberg $N_2(\Pi_u;\ v',\ J')$ states at $h\nu(VUV_1) < 117{,}184\ cm^{-1}$, Figures 3(a) and (b) show that the branching ratios for $N(^4S) + N(^2D)$ are near unity, except in the energy region from 113,121 to $113{,}709\ cm^{-1}$, where the competing $N(^4S) + N(^2P)$ channel becomes the major pathway with branching ratios in the range of 0.75–0.88. These correspond to the Q(1,2), R(0,1), and R(2) transitions of the valence $N_2(b^1\Pi_u;\ v' = 17–18)$ bands (see Figure 3(a) and Table 1). The spin-forbidden product channel $N(^4S) + N(^2P)$ was observed only weakly, with branching ratios $\leqslant 0.16$ at the R(0), R(1), and R(2) transitions of the Rydberg $N_2(c_4\,{}^1\Pi_u,\ v' = 0)$ band in the $h\nu(VUV_1)$ range of $115{,}569–115{,}577\ cm^{-1}$ (see Figure 3(b) and Table 2).

The lowest energy for the formation of the spin-allowed $N(^2D) + N(^2D)$ channel is observed when N_2 molecules are excited to the R(0,1) line of the $N_2(b'^1\Sigma_u^+,\ v' = 20)$ band at $117{,}206.9\ cm^{-1}$ (see Figure 3(c) and Table 3). This is only $\sim 45\ cm^{-1}$ above the threshold energy for the spin-allowed channel $N(^2D) + N(^2D)$, indicating that there is no potential barrier for this channel. The lowest Rydberg states that are observed to form this product channel are R(0) transitions of the bands $N_2(c_4{}^1\Pi_u,\ v' = 1)$ and $N_2(c_5{}'^1\Sigma_u^+;\ v' = 1)$ at 117,750.8 and $118{,}074.2\ cm^{-1}$, respectively, and they are 588.8 and $912.2\ cm^{-1}$ above the energetic threshold, respectively. The branching ratio curves of Figures 3(b)–(d) all show that the $N(^2D) + N(^2D)$ channel becomes the major dissociation pathway above its energetic threshold. Nevertheless, the spin-forbidden $N(^4S) + N(^2D)$ and $N(^4S) + N(^2P)$ channels for

Table 4
Product Branching Ratios for the $N(^4S) + N(^2D)$, $N(^4S) + N(^2P)$, and $N(^2D) + N(^2D)$ Channels from Excitation to the N_2 (c_4', c_5', c_6', and $c_7'^1\Sigma_u^+$; v', J') Rydberg States in N_2 Photodissociation

Term	v'	J''	VUV_1 (cm^{-1})	$N(^4S) + N(^2D)$	$N(^4S) + N(^2P)$	$N(^2D) + N(^2D)$
$c_4'(^1\Sigma_u^+)$	$v' = 0$	P(2)	104314.3	1.000	0.000	0.000
		P(1)	104318.4	1.000	0.000	0.000
		R(0)	104326.4	1.000	0.000	0.000
		R(1)	104330.1	1.000	0.000	0.000
		R(2)	104333.7	1.000	0.000	0.000
$c_4'(^1\Sigma_u^+)$	$v' = 1$	P(2)	106360.0	1.000	0.000	0.000
		P(1)	106364.6	1.000	0.000	0.000
		R(0)	106372.0	1.000	0.000	0.000
		R(1)	106374.8	1.000	0.000	0.000
		R(2)	106377.1	1.000	0.000	0.000
$c_4'(^1\Sigma_u^+)$	$v' = 2$	P(2)	108535.9	1.000	0.000	0.000
		P(1)	108541.0	1.000	0.000	0.000
		R(0)	108547.8	1.000	0.000	0.000
		R(1)	108549.6	1.000	0.000	0.000
		R(2)	108550.0	1.000	0.000	0.000
$c_4'(^1\Sigma_u^+)$	$v' = 3$	P(2)	110652.7	0.937[a](0.85)[b]	0.063[a](0.15)[b]	0.000
		R(0)	110659.9	0.943[a]	0.057[a]	0.000
		R(1)	110662.4	0.936[a]	0.064[a]	0.000
$c_4'(^1\Sigma_u^+)$	$v' = 4$	P(2)	112759.7	0.385 ± 0.016	0.615 ± 0.016	0.000
		P(1)	112764.2	0.390 ± 0.012 (0.606 ± 0.148)[c]	0.610 ± 0.012 (0.394 ± 0.148)[c]	0.000
		R(0)	112771.7	0.426 ± 0.037	0.574 ± 0.037	0.000
		R(1)	112774.2	0.410 ± 0.018 (0.517 ± 0.057)[c]	0.590 ± 0.018 (0.483 ± 0.057)[c]	0.000
		R(2)	112776.1	0.413 ± 0.021 (0.439 ± 0.045)[c]	0.587 ± 0.021 (0.561 ± 0.045)[c]	0.000
$c_4'(^1\Sigma_u^+)$	$v' = 5$	P(1)	114824.0	0.774 ± 0.024	0.226 ± 0.024	0.000
		R(0)	114834.8	1.000	0.000	0.000
		R(1)	114837.9	1.000	0.000	0.000
		R(2)	114839.9	1.000	0.000	0.000
$c_5'(^1\Sigma_u^+)$	$v' = 0$	R(0)	115851.8	0.367 ± 0.015 (0.36 ± 0.041)[c]	0.633 ± 0.0015 (0.64 ± 0.041)[c]	0.000
		R(0,2)	115853.4	0.386 ± 0.021	0.615 ± 0.021	0.000
$c_4'(^1\Sigma_u^+)$	$v' = 6$	R(0)	116810.3	0.725 ± 0.028	0.275 ± 0.028	0.000
		R(1)	116813.5	0.712[a]	0.288[a]	0.000
		R(2)	116816.1	1.000	0.000	0.000
$c_5'(^1\Sigma_u^+)$	$v' = 1$	R(0)	118074.2	0.000	0.000	1.000
$c_4'(^1\Sigma_u^+)$	$v' = 7$	R(0)	118770.7	0.011 ± 0.002	0.010 ± 0.001	0.979 ± 0.002
		R(1)	118771.9	0.008 ± 0.002	0.000	0.992 ± 0.002
$c_6'(^1\Sigma_u^+)$	$v' = 0$	R(0)	119944.5	0.000	0.000	1.000
$c_5'(^1\Sigma_u^+)$	$v' = 2$	R(0,1)	120194.3	0.450 ± 0.024	0.000	0.550 ± 0.024
$c_4'(^1\Sigma_u^+)$	$v' = 8$	R(0,1)	120689.0	0.369 ± 0.030	0.181 ± 0.019	0.450 ± 0.011
		R(2)	120693.5	0.226 ± 0.039	0.000	0.774 ± 0.049
$c_7'(^1\Sigma_u^+)$	$v' = 0$	R(0)	121870.0	0.353 ± 0.040	0.000	0.642 ± 0.040

Notes.
[a] Value determined by one ion image; the uncertainty is estimated to be 1%–3% based on the counting statistics.
[b] Reported by Walter et al. (1993).
[c] Reported by Cosby & Walter (1996).

some predissociative $^1\Pi$ and $^1\Sigma_u^+$ states remain competitive with the spin-allowed $N(^2D) + N(^2D)$ channel at an energy up to 4997 cm^{-1} beyond its energetic threshold.

By populating the valence states with $^1\Pi_u$ symmetry, the lowest energy observed for the formation of the $N(^4S) + N(^2P)$ channel was at the Q(2) line (109,826.1 cm^{-1}) of the $N_2(b^1\Pi_u; v' = 12)$ band (see Table 1 and the magnified branching ratio curve of Figure 3(a)). For exciting the valence N_2 states with $^1\Sigma_u^+$ symmetry, the lowest energy observed for the $N(^4S) + N(^2P)$ channel is at the R(2) transition (109,534.2 cm^{-1}) of the N_2 ($b'^1\Sigma_u^+$, $v' = 8$) band (see Table 3 and the magnified branching ratio curve of Figure 3(c)). Taking into account that the energetic threshold for the $N(^4S) + N(^2P)$ channel is 107,553 cm^{-1}, these experimental results suggest an upper bound for the potential energy barrier of 1981 cm^{-1} for the formation of $N(^4S) + N(^2P)$ products. This observation of a potential energy barrier is consistent with the expectation that the formation of the spin-forbidden $N(^4S) + N(^2P)$ products necessarily involves a singlet to triplet crossing (Ndome et al. 2008; Hochlaf et al. 2010b). By directly exciting the triplet $N_2(C^3\Pi_u; v' = 16, J')$ states, the lowest energy observed for this channel is found to be ≈108,290 cm^{-1}. This observation yields a lower upper bound value of ≈740 cm^{-1} for the potential barrier of the $N(^4S) + N(^2P)$ channel.

The present experiment shows that the branching ratios for the competing spin-forbidden channels, $N(^4S) + N(^2D)$ and $N(^4S) + N(^2P)$, of the valence $N_2(^1\Sigma_u^+)$ states exhibit oscillatory structures in the $h\nu(VUV_1)$ region below the

Table 5
Product Branching Ratios for the N(^{4}S) + N(^{2}D), N(^{4}S) + N(^{2}P), and N(^{2}D) + N(^{2}D) Channels from Excitation to Valence N_2 States, ($C^3\Pi_u$; $v' = 16$, J'), and Rydberg N_2 States, ($X^+(0)$ 4f), $X^+(0)$ 4f, ($X^+(1)$ 4f) and ($X^+(0)$ 5f), in N_2 Photodissociation

Term	v'	J''	VUV_1 (cm^{-1})	N(^{4}S)+N(^{2}D)	N(^{4}S)+N(^{2}P)	N(^{2}D)+N(^{2}D)
$C(^3\Pi_u)$	$v' = 16$	P(3)	108276.4	0.925 ± 0.005	0.075 ± 0.005	0.000
		P(2)	108283.6	0.887 ± 0.019	0.113 ± 0.019	0.000
		Q(2)	108288.2	0.954 ± 0.004	0.046 ± 0.004	0.000
		R(3)	108291.5	0.892 ± 0.015	0.108 ± 0.015	0.000
		R(0,1)	108295.5	0.959 ± 0.011	0.041 ± 0.011	0.000
$X^+(0)$ 4f, L = +3	$v' = 0$	Q(2), R(2)	118707.8	0.012 ± 0.007	0.000	0.988 ± 0.007
		P(2)	118710.4	0.000	0.000	1.000
		R(1)	118715.1	0.011 ± 0.006	0.000	0.989 ± 0.006
		R(0)	118722.3	0.006 ± 0.008	0.000	0.994 ± 0.008
$X^+(0)$ 4f, L = −3	$v' = 0$	P(1)	118726.5	0.070[a]	0.000	0.930[a]
$X^+(0)$ 4f, L =-1	$v' = 0$	R(2)	118787.8	0.008 ± 0.002	0.000	0.992 ± 0.002
$X^+(1)$ 4f, L = +3	$v' = 1$	P(2),Q(2),R(2)	120872.4	0.144 ± 0.019	0.000	0.856 ± 0.019
		R(1)	120878.8	0.302 ± 0.021	0.000	0.698 ± 0.021
		R(0)	120884.9	0.388 ± 0.193	0.000	0.612 ± 0.193
		Q(0)	120888.3	0.384 ± 0.008	0.000	0.616 ± 0.008
$X^+(0)$ 5f, L = +3	$v' = 0$	R(0)	121242.4	0.909 ± 0.003	0.000	0.091 ± 0.003
$X^+(0)$ 5f, L = −3	$v' = 0$	Q(0)	121274.5	0.872 ± 0.027	0.000	0.128 ± 0.027

Note.
[a] Value determined by a single ion image; the uncertainty is estimated to be 1%–3% based on the counting statistics.

energetic threshold of the N(^{2}D) + N(^{2}D) channel. Three oscillatory peaks of the branching ratio curve for the N(^{4}S) + N(^{2}P) channel located at 110,192.7 cm^{-1} [$N_2(b'^1\Sigma_u^+$; $v' = 9$)], 113,541.0 cm^{-1} [$N_2(b'^1\Sigma_u^+$; $v' = 14$)], and 116,678.4 cm^{-1} [$N_2(b'^1\Sigma_u^+$; $v' = 19$)] are clearly observed in Figure 3(c). These peak positions coincide with the minima positions of the branching ratio curve for the N(^{4}S) + N(^{2}D) channel, indicating the competitive nature of the two product channels. To our knowledge, these oscillatory structures have not been observed previously. The comparison of the branching ratio curves of Figures 3(a) and (c) shows that the two peaks at 110,192.7 and 113,541.0 cm^{-1} for N(^{4}S) + N(^{2}P) resolved in Figure 3(c) are also discernible in Figure 3(a), although the peak appearing near 110,192.7 cm^{-1} in Figure 3(a) is very weak. The two peaks at 113,541.0 and 116,678.4 cm^{-1} are also partially resolved in Figure 3(d) for the Rydberg N_2 states with $^1\Sigma_u^+$ symmetry, while no obvious oscillation of the branching curve is apparent in Figure 3(b) for the Rydberg N_2 states with $^1\Pi_u$ symmetry.

4.3. Theoretical Potential Energy Curves of Relevance to VUV Photodissociation of N_2

In order to provide insight to the experimental observation, theoretical ab initio PECs for N_2 states in the frequency range of 70,000–120,000 cm^{-1} calculated as a function of the N–N distance [r(N–N)] are shown in Figure 4. Since only ungerade states can be populated by VUV excitation from the gerade $N_2(X^1\Sigma_g^+)$ ground state, only PECs of the ungerade states are depicted in the figure. The $^1\Pi_u$ PECs are diabatic curves from Spelsberg & Meyer (2001). The most outstanding features of the PECs are the avoided crossings of $C^3\Pi_u$ and $C'^3\Pi_u$ at ≈101,250 cm^{-1}, $C'^3\Pi_u$ and $III^3\Pi_u$ at ≈113,573 cm^{-1}, and $b'^1\Sigma_u^+$ and $c'^1\Sigma_u^+$ at ≈110,000–116,000 cm^{-1}, which are marked by dashed circles in Figure 4. Vibronic couplings induce these avoided crossings. The dissociation along the PECs of $C^3\Pi_u$, $C'^3\Pi_u$, and $III^3\Pi_u$ (shown in green) leads to the formation of the N(^{4}S) + N(^{2}D), N(^{4}S) + N(^{2}P), and N(^{2}D) + N(^{2}D) channels, respectively. The potential energy diagram of Figure 4 shows that the PECs of states that correlate to the N(^{4}S) + N(^{4}S) ground-state channel are high-multiplicity states and cannot be populated readily from photoexcitation, indicating that the formation of the ground-state product channel is highly unfavorable, in accord with the present experimental findings.

The black vertical line marked as FC in Figure 4 shows the central Franck–Condon excitation region from $N_2(X^1\Sigma_g^+$; $v'' = 0$) at r(N–N) = 2.08 Bohr. The accessible VUV excited N_2 states with $^1\Pi_u$ symmetry [($b^1\Pi_u$; v'), ($c_n^1\Pi_u$; v'), and ($o_n^1\Pi_u$; v')] are shown in red, and those with $^1\Sigma_u^+$ symmetry [($b'^1\Sigma_u^+$; v') and ($c'_n{}^1\Sigma_u^+$; v')] are shown in blue. The initial formation of lower $^1\Sigma_u^+$ and $^1\Pi_u$ states by VUV excitation can populate the $b^1\Pi_u$ and $b'^1\Sigma_u^+$ states by vibronic couplings. Both these $b^1\Pi_u$ and $b'^1\Sigma_u^+$states correlate to the N(^{2}D) + N(^{2}D) channel. The $b^1\Pi_u$ can couple to the $C^3\Pi_u$ and $C'^3\Pi_u$ states by spin–orbit interactions at the $C^3\Pi_u/C'^3\Pi_u$ avoided crossing, leading to the formation of N(^{4}S) + N(^{2}D) products via the $C^3\Pi_u$ PEC. This is in agreement with the conclusion obtained by Lewis at al. (2005). The fact that the PECs for $b^1\Pi_u$ and $b'^1\Sigma_u^+$ states are nearly overlapping with the $C'^3\Pi_u$ state in the r(N–N) range of 2.5–4.0 Bohr can also promote spin–orbit interactions, resulting in the population of the $C'^3\Pi_u$ state that correlates to the N(^{4}S) + N(^{2}P) channel.

The $C^3\Pi_u$ PEC is predicted to have a potential barrier at the internuclear distance ≈3.6 Bohr. The top barrier of the $C^3\Pi_u$ PEC, which defines the barrier height for the N(^{4}S) + N(^{2}D) channel, is predicted to be close to the $N_2(b^1\Pi_u$; $v' = 0$) state located at 100,808 cm^{-1}. Since this state is the lowest predissociative state that can be populated by VUV excitation in the present experiment and the formation of N(^{4}S) + N(^{2}D) products is observed via this state, we conclude that the upper bound of the potential barrier for the N(^{4}S) + N(^{2}D) channel is 2870 cm^{-1}. Based on the coupled-channel calculations by Lewis et al., the shallow potential well formed between the $C^3\Pi_u/C'^3\Pi_u$ avoided crossing and the potential barrier at internuclear distance ≈3.6 Bohr can hold bound vibrational states, and they are predicted to be dissociative (Lewis et al.

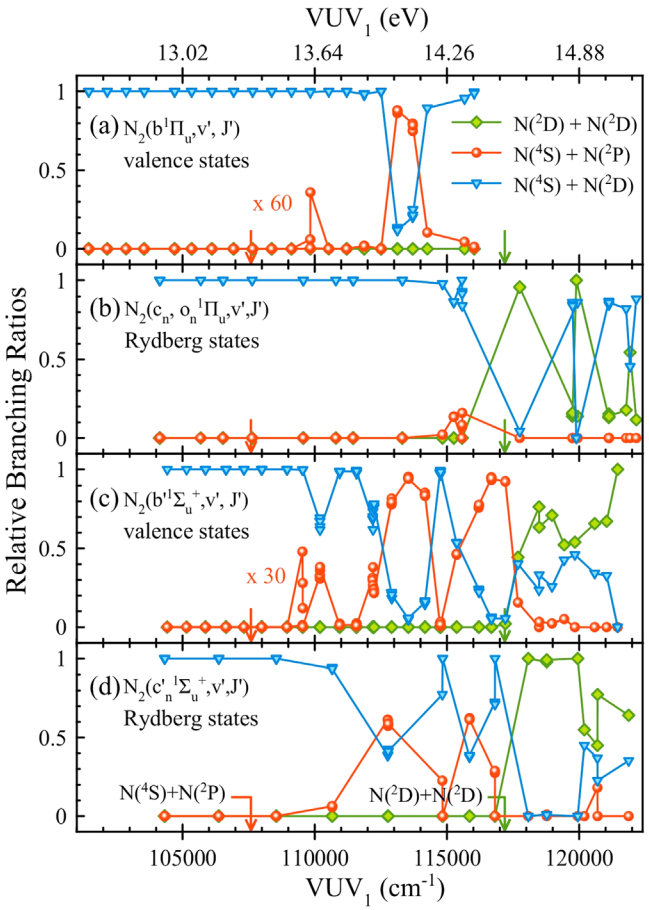

Figure 3. Branching ratios for the spin-forbidden N(^{4}S) + N(^{2}D) (blue) and N(^{4}S) + N(^{2}P) (red) channels and the spin-allowed N(^{2}D) + N(^{2}D) (green) channel observed in the photodissociation of N_2 in the $h\nu$(VUV$_1$) range of 100,500–122,200 cm^{-1}. This range covers excitation of (a) valence N_2 states with $^1\Pi_u$ symmetry, (b) Rydberg N_2 states with $^1\Pi_u$ symmetry, (c) valence N_2 states with $^1\Sigma_u^+$ symmetry, and (d) Rydberg N_2 states with $^1\Sigma_u^+$ symmetry. The downward-pointing red and green arrows mark the energetic thresholds of the N(^{4}S) + N(^{2}P) and N(^{2}D) + N(^{2}D) channels at 107,587.1 and 117.184.5 cm^{-1}, respectively. A respective 60-fold and 30-fold magnification of the *Y*-axes of the (a) and (c) branching ratio curves is shown to illustrate the threshold for the N(^{4}S) + N(^{2}P) channel.

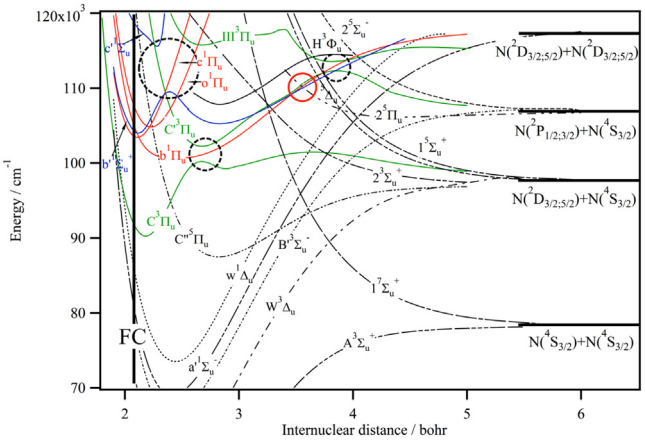

Figure 4. Ab initio PECs for the N_2 molecule in the energy range of 70,000–120,000 cm^{-1}. These PECs are computed at the CASSCF/MRCI/aug-cc-pVQZ(+3 s+2p) following procedures described in Ndome et al. (2008) and Hochlaf et al. (2010b). The vertical line marked FC represents the center Franck–Condon transition region. The PECs of the $^1\Pi_u$, $^1\Sigma_u^+$, and $^3\Pi_u$ states are shown in red, blue, and green, respectively. The $^1\Pi_u$ PECs are diabatic curves from Spelsberg & Meyer (2001). The $C^3\Pi_u/C'^3\Pi_u$, $C'^3\Pi_u/III^3\Pi_u$, and $b'^1\Sigma_u^+/c'^1\Sigma_u^+$ avoided crossings are marked by dashed circles. The dissociation along the $C^3\Pi_u$, $C'^3\Pi_u$, and $III^3\Pi_u$ states correlates with the dissociation channels N(^{4}S) + N(^{2}D), N(^{4}S) + N(^{2}P), and N(^{2}D) + N(^{2}D), respectively.

2005). This could lower the dissociation barrier for the N(^{4}S) + N(^{2}D) channel to about 1500 cm^{-1}.

As shown in Figure 4, higher $^1\Sigma_u^+$ states initially populated by VUV excitation in shorter r(N–N) range can couple with the $C'^3\Pi_u$ state by spin–orbit interactions as the $C'^3\Pi_u$ PEC passes through the $b'^1\Sigma_u^+/c'^1\Sigma_u^+$ avoided crossing region (marked by dashed circles). At sufficiently high energies above the potential barrier of the $b'^1\Sigma_u^+$ state, excited N_2 molecules initially prepared in $^1\Sigma_u^+$ states can also couple with the $^3\Pi_u$ states at the $C'^3\Pi_u/III^3\Pi_u$ avoided crossing, and then following the $C'^3\Pi_u$ PEC to produce N(^{4}S) + N(^{2}P) products. Based on the calculated PECs, the further excitation of $N_2(X^1\Sigma_g^+)$ to high $^1\Sigma_u^+$ states is expected to result in the formation of the N(^{2}D) + N(^{2}D) channel without a potential barrier. This prediction is also consistent with the experimental observation.

The theoretical calculations show that the $C'^3\Pi_u/III^3\Pi_u$ avoided crossing occurs at r(N–N) ≈3.47 Bohr, and the maximum of the $C'^3\Pi_u$ PEC is located at ≈112,500 cm^{-1}, giving a value of ≈4950 cm^{-1} for the potential barrier for the formation of N(^{4}S) + N(^{2}P) products. However, this value is much higher than the estimate of ≈740 cm^{-1} obtained in the present experiments by exciting the predissociative triplet $N_2(C^3\Pi_u; v' = 16, J')$ states. Figure 4 shows that the $2^5\Pi_u$ and $C'^3\Pi_u$ states intersect at ≈110,000 cm^{-1} and r(N–N) ≈ 3.5 Bohr (marked by a red circle). Since the $2^5\Pi_u$ state leads directly to N(^{4}S) + N(^{2}P) products, a further conversion from the triplet $C'^3\Pi_u$ to the quintet $2^5\Pi_u$ state by spin–orbit coupling would lower the predicted potential barrier for this channel to ≈2450 cm^{-1}. However, the latter value remains significantly higher than the experimental value of ≈740 cm^{-1}. The large discrepancy observed between the theoretical and experimental potential barriers for the formation of the N(^{4}S) + N(^{2}P) channel is indicative of more complex pathways, which may involve multiple crossings or other quantum coupling mechanisms (Lewis et al. 2005).

The theoretical PECs have provided insight for the oscillations observed in the branching ratio curves in Figures 3(a) and (c). The photodissociation cross section of N_2 depends on the Franck–Condon factor for photoexcitation, as well as the strength of electronic couplings of the excited states involved. The oscillations of the branching ratios as observed for the $N_2(b^1\Pi_u; v' = 0–23)$ and $N_2(b'^1\Sigma_u^+; v' = 0–28)$ bands may be due to the variations of the integrals of vibrational wavefunctions. The theoretical PECs of Figure 4 show that the singlet $b^1\Pi_u$ and $b'^1\Sigma_u^+$ states run parallel to the triplet $C'^3\Pi_u$ state so that the couplings between these states should depend on the vibrational overlap integrals between them over the r(N–N) range of 2.5–4.0 Bohr.

The peaks observed in the branching ratio curves for the N(^{4}S) + N(^{2}P) channel located at $h\nu$(VUV$_1$) ≈ 113,541.0 cm^{-1} coincide with the location of the $C'^3\Pi_u/III^3\Pi_u$ avoided crossing, indicating that the formation of N(^{4}S) + N(^{2}P) products is strongly favored from dissociative valence N_2 states situated at this energy gap. The lowest energy to the N(^{4}S) + N(^{2}P) channel located at 110,192.7 cm^{-1} was also found to coincide with the energy position at which the $C'^3\Pi_u$ and $2^5\Pi_u$ states

intersect. The highest-energy branching ratio peak observed at $h\nu(\mathrm{VUV}_1) \approx 116{,}678.4\ \mathrm{cm}^{-1}$ for the $N(^4S) + N(^2P)$ channel could be ascribed to a higher efficiency for excitation to the $(c'^1\Sigma_u^+;\ v')$ state, which subsequently couples via spin–orbit interaction to the $C'^3\Pi_u$ state, leading to the formation of the $N(^4S) + N(^2P)$ channel. It appears from the experiment that for the production of the $N(^4S) + N(^2P)$ channel, excitation to the $N_2(b'^1\Sigma_u^+;\ v')$ states is more effective compared to the $N_2(b^1\Pi;\ v')$ states. This observation could be rationalized that the $N_2(b'^1\Sigma_u^+;\ v')$ states can couple to the $C'^3\Pi_u$ state at short as well as long r(N–N) ranges, whereas the $N_2(b^1\Pi_u;v')$ states couple to the $C'^3\Pi_u$ state mostly in the long r(N–N) range.

In the present study, we are mainly focusing on reporting the experimental branching ratios of N_2 photodissociation over a very large photon energy range and theoretically explaining the overall trend of these ratios as the vibrational energy of the excited states changes. Our branching ratios are for low-J' (mainly $J' = 0$–3) states since a cold N_2 molecular beam is generated by supersonic expansion. This is extremely useful in decoupling the spin–orbit interactions from rotational interactions when trying to explain the dissociation process theoretically. We have also measured the anisotropy parameters (or beta parameters) for the recoiling N atoms, which can be used in the theoretical model built by Buijsse and van der Zande (Buijsse et al. 1996; Buijsse & van der Zande 1997b) to provide more details of the dissociation dynamics. Detailed theoretical calculations and discussions of all the individual rotational states measured in the present experiment are beyond the scope of this paper and will be presented in separate publications.

4.4. Implications for Astronomy and Planetary Sciences

Nitrogen molecules have always been known to be important in the atmospheres of the planets, their satellites, and the early history of our solar system (Torr & Torr 1979, 1982; Strobel & Shemansky 1982; Meier 1991; Feldman et al. 2001; Bakalian 2006), but their importance in extrasolar planets, the interstellar medium, circumstellar envelopes, and comets has only been recognized recently (Knauth et al. 2004; Snow 2004; van Dishoeck 2006; Moses et al. 2011; Balucani 2012; Li et al. 2013, 2014). Thus, the branching ratios that we have obtained here are important in all of these regions, and they depend on both the intensity and the energy distributions of the VUV radiation striking the region. There are two energy regions that have to be considered, namely, above and below the $\mathrm{IE(H)} = 109{,}678.8\ \mathrm{cm}^{-1}$. When the VUV radiation illuminates a region that contains many H atoms, only the radiation below the IE(H) will be important because H atoms will absorb all the radiation with energies above $109{,}678.8\ \mathrm{cm}^{-1}$. Considering the branching ratios in Figures 3(a)–(d), it is clear that only $N(^4S) + N(^2D)$ atoms are formed, and they have a maximum available recoil energy of 1.46 eV or 0.73 eV/atom. This translational recoil energy is not enough to drive the reactions of the $N(^4S)$ atoms with H_2 and other molecules, but it will be enough for the $N(^2D)$ atoms to overcome any activation energy that is associated with chemical reactions between this atom and any other molecules that might be present (Herron 1999; Pascual et al. 2002). In those astronomical regions where light with energies above $109{,}678.8\ \mathrm{cm}^{-1}$ can penetrate, Reaction (4) becomes more important since two $N(^2D)$ are produced for every photon absorbed. These $N(^2D)$ have a lower recoil translational energy since a significant amount of the available energy has gone into excitation of the second N atom. At these higher energies the N (^2P) are also produced, but these atoms are considerably less reactive than $N(^2D)$ atoms (Herron 1999).

The lifetimes for the radiative decay of the excited $N(^2D_J$, $J = 3/2$ and $5/2$) spin–orbit states to the $N(^4S_{3/2})$ ground state have values of 13.69 and 36.67 hr, respectively, because they are spin-forbidden processes (Godefroid & Fischer 1984). The $N(^2P_J$, $J = 1/2$ and $3/2$) atoms undergo faster radiative decay to both $N(^2D_{3/2})$ and $N(^2D_{5/2})$ states with lifetimes of 52.9 and 47.9 s, respectively (Godefroid & Fischer 1984). When the total number densities for molecular species in astronomical regions are greater than $10^8\ \mathrm{cm}^{-3}$, the reactions of the $N(^2P_J)$ state have to be considered because the collision time is shorter than the radiative lifetimes of these states. Since these excited atoms are considerably less reactive, they will probably only undergo energy transfer to the $N(^2D)$ and $N(^4S)$ states.

5. COMETARY IMPLICATIONS

The observation of N_2 in comet 67/P Churyumov-Gerasimenko (67/P CG) by the ROSINA mass spectrometer on the *Rosetta* spacecraft when the comet was ≈3 AU from the Sun proves that this molecule is present in comets (Rubin et al. 2015). Satellite observations of numerous comets have shown that the dust and gas come out from the nucleus as jets similar to the jets formed in the laboratory from free expansion of a gas into a vacuum system. So like we have shown in this paper, N_2 coming out of such jet will be exposed to solar radiation below 100 nm, and it is likely to dissociate to form $N(^2D)$ atoms that are highly energetic and long-lived. Once these atoms are formed, they are likely to collide and react with H_2O molecules depending on the astronomical region that is being discussed. The recommended rate constant for the reaction of $N(^2D)$ atoms with H_2O is about $4 \times 10^{-11}\ \mathrm{cm}^3\ \mathrm{molecules}^{-1}\ \mathrm{s}^{-1}$ (Umemoto et al. 1999). The expected products for this reaction are NH + OH, H + HNO, and H_2 + NO (Umemoto et al. 1999; Casavecchia et al. 2001). Collisions of both $N(^2D)$ and $N(^2P)$ atoms with H_2O molecules can lead to energy transfer between these metastable atoms and the H_2O that could then cascade down to the metastable 6_{16} level of H_2O that may have been detected in several comets and the interstellar medium (Jackson et al. 1976; Altenhoff et al. 1983; Bird et al. 1997; Cosmovici et al. 1998, 2014; Cottin et al. 1999). Whether or not collisions of long-lived $N(^2D)$ and $N(^2P)$ atoms are important in explaining the later observations, it is clear that they are important in understanding the overall process in astronomical bodies.

6. CONCLUSIONS

The branching ratios are measured for the $N(^4S) + N(^2D)$, $N(^4S) + N(^2P)$, and $N(^2D) + N(^2D)$ product channels from VUV photodissociation of N_2 over a wide energy range from 100,808 to $122{,}159\ \mathrm{cm}^{-1}$. Comparisons between the current experimental measurements and those measured by Cosby and coworkers (Helm & Cosby 1989; Walter et al. 1993, 1994; Cosby & Walter 1996) are made for states with common rovibrational quantum numbers, and they are found to be in general agreement with each other. This energy range covers four sets of singlet predissociative N_2 rovibronic states, namely, the $(^1\Pi_u;\ v', J')$ and $(^1\Sigma_u^+;\ v', J')$ valence and Rydberg states, as well as the $N_2(C^3\Pi_u;\ v' = 16,\ J')$ states. The fact that the

branching ratio curves obtained for the four sets of singlet N_2 states in this common energy range are distinctly different indicates that the branching ratios are dependent on the N_2 predissociative state and the photodissociation of N_2 is nonstatistical.

No experimental evidence for the production of the spin-allowed $N(^4S) + N(^4S)$ ground-state channel is seen, in agreement with previous experimental measurements (Helm & Cosby 1989; Walter et al. 1993, 1994). The spin-allowed $N(^2D) + N(^2D)$ channel occurs with no potential barrier and eventually becomes the dominant process at 4173 cm^{-1} above its energetic threshold.

In the energy region between the energetic thresholds for the $N(^4S) + N(^2P)$ and $N(^2D) + N(^2D)$ channels both the spin-forbidden $N(^4S) + N(^2D)$ and $N(^4S) + N(^2P)$ channels occur. The branching ratios for these channels exhibit oscillatory structures, when plotted as a function of $h\nu(VUV_1)$ for the excitation of the $(^1\Pi_u; v', J')$ and $(^1\Sigma_u{}^+; v', J')$ valence and Rydberg states. This indicates that the dominant production of the $N(^4S) + N(^2D)$ or $N(^4S) + N(^2P)$ or $N(^2D) + N(^2D)$ channels can be controlled by photoexcitation to selected N_2 rovibronic states.

High-level ab initio PECs for the N_2 states calculated in the energy range between 70,000 and 120,000 cm^{-1} predict that the formation of both spin-forbidden channels $N(^4S) + N(^2D)$ and $N(^4S) + N(^2P)$ involves potential barriers. The theoretical PECs suggest that by taking into account the spin–orbit interaction of the $C'^3\Pi_u$ and $2^5\Pi_u$ states, the theoretical potential barrier can be lower for the $N(^4S) + N(^2P)$ channel, putting it in closer agreement with the experimental measurements. The determination of the potential barrier for the $N(^4S) + N(^2D)$ channel is limited by the lowest state $[N_2(b^1\Pi_u; v' = 0)]$ that can be prepared by VUV photoexcitation. Nevertheless, the upper bound of 2870 cm^{-1} for the potential barrier of the $N(^4S) + N(^2D)$ channel obtained here is close to the theoretical prediction based on the PEC curves shown in Figure 4. The oscillatory peaks observed in the branching ratio curves for the $N(^4S) + N(^2P)$ channel have also been rationalized based on the calculated PECs.

W.M.J. is grateful for the support provided under NSF grant No. CHE-1301501 and acknowledges the insightful discussions with Alan Heays on the $N_2(C^3\Pi_u, v' = 16)$. C.Y.N. is supported by the NSF grant No. CHE-1462172. M.H. is thankful for a Marie Curie International Research Staff Exchange Scheme Fellowship under grants No. PIRSES-GA-2012-31754 and the COST Action CM1405 MOLIM. The theoretical calculation of this study was undertaken while M.H. was a Visiting Professor at King Saud University.

REFERENCES

Altenhoff, W. J., Batrla, W., Huchtmeier, W. K., et al. 1983, A&A, 125, L19
Bakalian, F. 2006, Icar, 183, 69
Balucani, N. 2012, Chemical Society Reviews, 41, 5473
Berning, A., Schweizer, M., Werner, H.-J., Knowles, P. J., & Palmieri, P. 2000, MolPh, 98, 1823
Bird, M. K., Janardhan, P., Wilson, T. L., et al. 1997, EM&P, 78, 21
Buijsse, B., & van der Zande, W. J. 1997a, FaDi, 108, 271
Buijsse, B., & van der Zande, W. J. 1997b, JChPh, 102, 9447
Buijsse, B., Wouters, E. R., & van der Zande, W. J. 1996, PhRvL, 77, 243
Carroll, P. K., & Collins, C. P. 1969, CaJPh, 47, 563
Carroll, P. K., & Mulliken, R. S. 1965, JChPh, 43, 2170
Casavecchia, P., Balucani, N., Cartechini, L., et al. 2001, FaDi, 119, 27
Cosby, P. C., & Walter, C. W. 1996, in Fall Meeting of the American Geophysical Union (Washington, DC: AGU)
Cosmovici, C. B., Montebugnoli, S., Orfei, A., Pogrebenko, S., & Cortiglioni, S. 1998, P&SS, 46, 467
Cosmovici, C. B., Pluchino, S., Montebugnoli, S., & Pogrebenko, S. 2014, P&SS, 96, 22
Cottin, H., Gazeau, M. C., & Raulin, F. 1999, P&SS, 47, 1141
Dressler, K. 1969, CaJPh, 47, 547
Dunning, T. H. 1989, JChPh, 90, 1007
Feldman, P. D., Feldman, D. J., Kruk, J. W., Murphy, E. M., & Moos, H. W. 2001, JGRA, 106, 8119
Gao, H., Song, Y., Jackson, W. M., & Ng, C. Y. 2013, JChPh, 138, 191102
Gao, H., Yang, L., Pan, Y., et al. 2011, JChPh, 135, 134319
Godefroid, M., & Fischer, C. F. 1984, JPhB, 17, 681
Helm, H., & Cosby, P. C. 1989, JChPh, 90, 4208
Herron, J. T. 1999, JPCRD, 28, 1453
Hochlaf, M., Ndome, H., & Hammoutène, D. 2010a, JChPh, 132, 104310
Hochlaf, M., Ndome, H., Hammoutène, D., & Vervloet, M. 2010b, JPhB, 43, 245101
Jackson, W. M., Clark, T., & Donn, B. 1976, in NASA SP-393272, The Study of Comets (Washington, DC: NASA), 272
Kendall, R. A., Dunning, T. H., & Harrison, R. J. 1992, JChPh, 96, 6796
Knauth, D. C., Andersson, B. G., McCandliss, S. R., & Warren Moos, H. 2004, Natur, 429, 636
Knowles, P. J., & Werner, H.-J. 1985, CPL, 115, 259
Knowles, P. J., & Werner, H.-J. 1988, CPL, 145, 514
Kramida, A., Ralchenko, Y., Reader, J., & Team, N. A. 2014, (Gaithersburg, MD: National Institute of Standards and Technology) http://www.nist.gov/pml/data/asd.cfm
Lewis, B. R., Baldwin, K. G. H., Sprengers, J. P., et al. 2008a, JChPh, 129, 164305
Lewis, B. R., Gibson, S. T., Zhang, W., et al. 2005, JChPh, 122, 144302
Lewis, B. R., Heays, A. N., Gibson, S. T., et al. 2008b, JChPh, 129, 164306
Li, X., Heays, A. N., Visser, R., et al. 2013, A&A, 555, A14
Li, X., Millar, T. J., Walsh, C., Heays, A. N., & van Dishoeck, E. F. 2014, A&A, 568, A111
Llusar, R., Casarrubios, M., Barandiarán, Z., & Seijo, L. 1996, JChPh, 105, 5321
Lu, Z., Chang, Y. C., Yin, Q.-Z., Ng, C. Y., & Jackson, W. M. 2014, Sci, 346, 61
Meier, R. R. 1991, SSRv, 58, 1
Moses, J. I., Visscher, C., Fortney, J. J., et al. 2011, ApJ, 737, 15
Ndome, H., Hochlaf, M., Lewis, B. R., et al. 2008, JChPh, 129, 164307
Pan, Y., Gao, H., Yang, L., et al. 2011, JChPh, 135, 071101
Pascual, R. Z., Schatz, G. C., Lendvay, G., & Troya, D. 2002, JPCA, 106, 4125
Roncin, J.-Y., Subtil, J.-L., & Launay, F. 1998, JMoSp, 188, 128
Rubin, M., Altwegg, K., Balsiger, H., et al. 2015, Sci, 348, 232
Snow, T. P. 2004, Natur, 429, 615
Song, Y., Gao, H., Ng, C. Y., & Jackson, W. M. 2012, in EAS Publications Series 58295 (Cambridge: Cambridge Univ. Press)
Spelsberg, D., & Meyer, W. 2001, JChPh, 115, 6438
Strobel, D. F., & Shemansky, D. E. 1982, JGRA, 87, 1361
Torr, D. G., & Torr, M. R. 1979, JATP, 41, 797
Torr, M. R., & Torr, D. G. 1982, RvGeo, 20, 91
Umemoto, H., Asai, T., Hashimoto, H., & Nakae, T. 1999, JPCA, 103, 700
van Dishoeck, E. F. 2006, PNAS, 103, 12249
Walter, C. W., Cosby, P. C., & Helm, H. 1993, JChPh, 99, 3553
Walter, C. W., Cosby, P. C., & Helm, H. 1994, PhRvA, 50, 2930
Werner, H. J., & Knowles, P. J. 1985, JChPh, 82, 5053
Werner, H. J., & Knowles, P. J. 1988, JChPh, 89, 5803
Werner, H.-J., Knowles, P. J., Knizia, G., et al. 2012, https://www.molpro.net
Woon, D. E., & Dunning, T. H. 1995, JChPh, 103, 4572
Yoshino, K., Tanaka, Y., Carroll, P. K., & Mitchell, P. 1975, JMoSp, 54, 87
Zeng, T., Fedorov, D. G., Schmidt, M. W., & Klobukowski, M. 2011, JChPh, 134, 214107